



Cite this: *EES Catal.*, 2025,  
3, 843

## Elevated temperature and pressure driven ampere-level $\text{CO}_2$ electroreduction to CO in a membrane electrode assembly electrolyzer†

Yang Li, Huiyue Liu, Jithu Raj, Mohammad Pishnamazi and Jingjie Wu \*

Achieving high selectivity for carbon monoxide (CO) in the electrochemical reduction of carbon dioxide ( $\text{CO}_2$ ) at industrially relevant current densities, particularly using dilute  $\text{CO}_2$  feedstocks, remains a significant challenge. Herein, we demonstrate that combining elevated temperature and  $\text{CO}_2$  pressure substantially enhances CO production in a membrane electrode assembly (MEA) electrolyzer using commercially available silver nanoparticles. Elevated  $\text{CO}_2$  pressures increase  $\text{CO}_2$  concentration and reduce the diffusion layer, counteracting the reduced  $\text{CO}_2$  solubility in water and enhanced wetting of catalyst layer caused by high temperature. The synergy of high pressure and temperature ensures high  $\text{CO}_2$  flux to the catalyst surface while leveraging elevated temperatures to accelerate reaction kinetics. Therefore, the pressurized and heated  $\text{CO}_2$  electrolyzer achieves an  $\text{FE}_{\text{CO}}$  of 92% at a high current density of  $2 \text{ A cm}^{-2}$  and a low cell voltage of 3.8 V under 10 bar and 80 °C when using 0.1 M  $\text{KHCO}_3$  as the anolyte. Even when using pure water as the anolyte, the system maintains a  $\text{FE}_{\text{CO}}$  value of 90% at  $300 \text{ mA cm}^{-2}$  and a cell voltage of 3.6 V. Furthermore, the system demonstrates exceptional performance with dilute 10 vol%  $\text{CO}_2$  feedstocks, achieving a  $\text{FE}_{\text{CO}}$  of 96% at  $100 \text{ mA cm}^{-2}$  and 2.4 V. These findings underscore the potential of combined temperature and pressure optimization to overcome mass transport limitations and enhance reaction kinetics, offering a viable pathway for scaling up  $\text{CO}_2$  electrolyzers for industrial applications.

Received 4th February 2025,  
Accepted 16th April 2025

DOI: 10.1039/d5ey00034c

rsc.li/eescatalysis

### Broader context

Efforts to mitigate the adverse effects of carbon dioxide emissions while meeting global energy demands have driven extensive research in carbon capture and utilization technologies. The electrochemical  $\text{CO}_2$  reduction reaction ( $\text{CO}_2\text{RR}$ ) has emerged as a promising pathway to convert  $\text{CO}_2$  into valuable products such as carbon monoxide, formate, and hydrocarbons using renewable electricity. Among these, CO is particularly attractive due to its versatility in producing chemicals and fuels with positive technoeconomic potential. Advancements in the  $\text{CO}_2\text{RR}$ , particularly under industrially relevant conditions, hold the potential to revolutionize sustainable energy and environmental catalysis by reducing reliance on fossil fuels and lowering greenhouse gas emissions. The successful integration of optimized reaction parameters, such as high pressure and temperature, addresses mass transport and kinetic limitations, advancing scalable solutions for industrial  $\text{CO}_2$  conversion. As renewable-powered  $\text{CO}_2$  electrolyzers are developed, they could seamlessly integrate with  $\text{CO}_2$  capture systems, offering a circular carbon economy that aligns with decarbonization goals.

## 1. Introduction

In response to the escalating carbon dioxide ( $\text{CO}_2$ ) emissions driven by increased fossil fuel consumption,  $\text{CO}_2$  capture and utilization has become a global priority with accelerated research efforts.<sup>1</sup> The electrochemical  $\text{CO}_2$  reduction reaction

( $\text{CO}_2\text{RR}$ ) presents a dual function to mitigate greenhouse gas emissions and generate sustainable feedstocks by integrating with renewable electricity.<sup>2</sup> By tailoring the catalyst, reaction environment, and operating potential, the  $\text{CO}_2\text{RR}$  enables the production of a wide array of valuable products.<sup>3–6</sup> Among these, carbon monoxide (CO) stands out as a versatile feedstock for downstream upgrading to various hydrocarbon chemicals and fuels with promising market potential. Technoeconomic assessments indicate that CO is among the few  $\text{CO}_2\text{RR}$  products capable of achieving positive gross margins.<sup>7</sup> Extensive research has identified silver (Ag) as an optimal catalyst for selective CO production, yet achieving high CO selectivity at a

Department of Chemical and Environmental Engineering, University of Cincinnati, Cincinnati, OH 45221, USA. E-mail: jingjie.wu@uc.edu

† Electronic supplementary information (ESI) available: Additional information of the schematic of setup; calculated thermodynamic potential; temperature effect on diffusivity of  $\text{CO}_2$  in water, solubility of  $\text{CO}_2$ ,  $\text{K}_2\text{CO}_3$  and  $\text{KHCO}_3$ ; and electrochemical results. See DOI: <https://doi.org/10.1039/d5ey00034c>



high current density ( $>1 \text{ A cm}^{-2}$ ) remains a significant challenge due to the high energy barrier of  $\text{CO}_2$  activation and sluggish kinetics of multi-electron/proton transfer steps.<sup>8</sup>

A significant advancement in  $\text{CO}_2\text{RR}$  systems was achieved with the introduction of gas diffusion electrodes (GDEs), which effectively reduce the diffusion layer of gas phase  $\text{CO}_2$ , thereby enabling operation at industrially relevant current densities.<sup>9–11</sup> Among various cell configurations, the membrane electrode assembly (MEA) cell stands out as a promising approach, integrating GDEs to offer low ohmic resistance and scalability potential for multicell stacks.<sup>12,13</sup> It is widely considered that,<sup>14</sup> under operating conditions, the catalyst layer pores become saturated with liquid electrolyte, limiting the reaction primarily to the aqueous phase *via* dissolved  $\text{CO}_2$ .<sup>15–17</sup> However, high current densities often induce electrode flooding that thickens the diffusion layer of  $\text{CO}_2$ , posing mass transfer limitation in MEA cells. Efforts to overcome these current density limitations have primarily focused on modifying the catalyst layer by incorporating with materials such as polytetrafluoroethylene (PTFE) to enhance hydrophobicity, silicon dioxide ( $\text{SiO}_2$ ) to consume the hydroxide ions and thereby reducing the local pH, and cesium ( $\text{Cs}^+$ ) with induced electric field to lower the barrier of  $\text{CO}_2$  activation at high current densities.<sup>18–20</sup> Despite these advances, there has been comparatively little exploration of process intensification. To date, most  $\text{CO}_2\text{RR}$ -MEA cell studies have been conducted under ambient conditions, with only limited reports on investigating pressurized MEA cells.<sup>21,22</sup> In these studies, pressure was typically applied only to the cathode side, leading to gas crossover through the membrane due to pressure imbalances when the differential exceeded 6 bar, ultimately resulting in decreased performance.<sup>23</sup>

On the other hand, increasing the reaction temperature enhances  $\text{CO}_2\text{RR}$  kinetics, as the rate generally increases exponentially with temperature.<sup>24,25</sup> Industrial  $\text{CO}_2$  electrolyzers are expected to operate under elevated temperatures due to heat generated by overpotentials, resistive losses, as well as the high temperatures of flue gas streams, often exceeding 100 °C.<sup>26,27</sup> However, as temperature rises,  $\text{CO}_2$  solubility in aqueous electrolytes decreases, where the hydrogen evolution reaction (HER) tends to accelerate, complicating the optimization of  $\text{CO}_2\text{RR}$  selectivity.<sup>28</sup> Several studies have examined the effects of temperature on GDE-based  $\text{CO}_2\text{RR}$  systems with varying results depending on catalysts and cell configurations. For instance, in MEA cells using Ag catalysts, rising temperatures have been associated with reduced  $j_{\text{CO}}$  and  $\text{FE}_{\text{CO}}$  at reported cell voltages of 2.2–3.4 V, largely attributed to diminished  $\text{CO}_2$  adsorption, lower solubility, and increased water presence.<sup>21,23</sup> Conversely, under constant current conditions (100–500  $\text{mA cm}^{-2}$ ), elevated temperatures have been shown to enhance  $\text{FE}_{\text{CO}}$ .<sup>19</sup> In flow cell systems, peak  $\text{FE}_{\text{CO}}$  occurred at moderate temperatures under certain current, with performance declining at higher temperatures due to  $\text{CO}_2$  solubility constraints.<sup>29</sup> For Au catalysts,  $\text{FE}_{\text{CO}}$  generally decreased with increasing temperature under both constant potential ( $-0.7 \text{ V}_{\text{RHE}}$  in the flow cell) and constant current conditions (100  $\text{mA cm}^{-2}$  in the MEA cell), consistent with  $\text{CO}_2$  solubility limitations.<sup>30,31</sup> Similarly, Sn-based catalysts exhibited a decline in formate selectivity at higher temperatures in both flow cell and

MEA cell systems under the same cell voltage of 2.2 V, although partial current densities of formate plateau at elevated temperatures in MEA systems.<sup>25</sup> Notably, these previous studies often focused on a single cell voltage or a narrow temperature range at ambient pressure, leaving a gap in the understanding of how combined temperature and pressure impacts catalytic performance across varying cell voltages. Given that practical  $\text{CO}_2$  electrolyzers are expected to operate at elevated temperatures and pressures for seamless integration with upstream and downstream processes,<sup>32,33</sup> a systematic investigation into the interplay of these parameters on  $\text{CO}_2\text{RR}$  performance is essential to advance catalyst and electrode design as well as intensifying process operation.

In this work, by systematically varying reaction temperature and pressure using a commercial Ag catalyst in a MEA cell, we demonstrate the synergy of high temperature and pressure operation to drive the  $\text{CO}_2$ -to-CO conversion at simultaneously high current density and selectivity. Our results reveal that (i) high-pressure operation effectively enhances  $\text{CO}_2$  availability and promotes selective  $\text{CO}_2$  adsorption, thus facilitating the  $\text{CO}_2\text{RR}$  at high current density while suppressing the parasitic HER; (ii) the effect of temperature on  $j_{\text{CO}}$  is strongly influenced by the cell voltage and  $\text{CO}_2$  partial pressure. At lower cell voltages and higher  $\text{CO}_2$  pressures, elevated temperatures positively improve the CO formation rate. The combined effects of high temperature and pressure achieve an impressive  $\text{FE}_{\text{CO}}$  exceeding 92% at a current density of 2  $\text{A cm}^{-2}$  at a cell voltage of 3.8 V when using 0.1 M  $\text{KHCO}_3$  as the anolyte, a stark improvement over that under ambient conditions, where  $\text{FE}_{\text{CO}}$  drops from 95% at 100  $\text{mA cm}^{-2}$  to 73% at 200  $\text{mA cm}^{-2}$ . Additionally, pressurized and high-temperature operation presents a compelling strategy to substantially enhance  $\text{CO}_2\text{RR}$  performance when using pure water as the anodic feedstock or processing under dilute  $\text{CO}_2$  concentrations.

## 2. Experimental section

### 2.1. Chemicals

Potassium bicarbonate ( $\text{KHCO}_3$ , 99.7%) and potassium hydroxide (KOH, 99.99%) were purchased from Sigma-Aldrich and used as received without further purification. Silver nanoparticles (Ag, 20–40 nm) were purchased from Thermo Scientific. All solutions were prepared using Milli-Q water (17.8  $\text{M}\Omega \text{ cm}$ ).

### 2.2. Preparation of the Ag electrode

The Ag electrodes were fabricated using a standard air-brush technique. Initially, the Ag catalyst ink was prepared by dispersing Ag nanoparticles (40 mg) in iso-propanol (4 mL), followed by sonication for 30 minutes. The resulting ink was uniformly air-brushed onto carbon paper (Sigracet GDL 34BC, Fuel Cell Store) to achieve a catalyst loading of approximately 0.8  $\text{mg cm}^{-2}$ . The geometric area of the GDE cathode was 1.0  $\text{cm} \times 1.0 \text{ cm}$ .



### 2.3. Electrochemical measurements

The CO<sub>2</sub>RR performance under varying temperatures and pressures was evaluated in a MEA cell with 0.1 M KHCO<sub>3</sub> as the anolyte. The GDE cathode and an IrO<sub>2</sub>/Ti felt anode were separated by a PiperION anion exchange membrane (AEM, 20 µm, Fuel Cell Store). For the pure CO<sub>2</sub>RR, dry CO<sub>2</sub> gas was supplied to the cathode at a flow rate of 250 sccm via a mass flow controller (Alicat Scientific) without external humidification. For the diluted CO<sub>2</sub>RR, a CO<sub>2</sub>/N<sub>2</sub> gas mixture was used, with the total mass flow controlled at 250 sccm. For instance, for 10 vol% CO<sub>2</sub>RR, 25 sccm of CO<sub>2</sub> was mixed with 225 sccm of N<sub>2</sub>, whereas for 50 vol% CO<sub>2</sub>RR, 125 sccm of CO<sub>2</sub> was mixed with 125 sccm of N<sub>2</sub>. A potentiostat (Gamry Interface 5000E) was used to apply a constant current to the MEA cell and record the corresponding cell voltage without *iR* correction. The cell temperature was controlled by electrical heating rods directly connected to both the cathode and anode flow fields, with a thermocouple inserted into the cell to maintain the desired temperature (Fig. S1, ESI<sup>†</sup>), which was regulated by a PID temperature controller (Cole-Parmer TC5000).

A schematic and photograph of the pressure setup is shown in Fig. S2 and S3 (ESI<sup>†</sup>). In all pressurized MEA setups, the pressures on the cathode and anode sides were balanced to ensure consistent conditions. The anode side pressure was controlled using a back-pressure regulator (BPR, Equilibar model LF2 with PEEK non-reinforced diaphragm) downstream of the cell, equipped with a high-pressure electronic pilot controller (Equilibar). The anolyte was fed into the anode using a high-pressure syringe pump (Fusion 6000X, Chemtex) at a flow rate of 0.5 mL min<sup>-1</sup>. As for the cathode side, gas pressure was maintained using stacked back-pressure regulators (Swagelok, KPB1J0A4A5A20000). A cold trap was positioned downstream of the cathode effluent to separate gaseous and liquid products. Due to liquid product crossover, the FEs of the liquid products were calculated based on the total amount collected from both the anode and cathode sides during the same time period. Gas samples were collected downstream of the BPR, ensuring that the gas was at atmospheric pressure.

### 2.4. Product detection

During the electrochemical reaction, an in-line gas chromatograph (GC, Agilent 8860) was employed to monitor gaseous products. To calibrate the outlet gas flow rate of CO<sub>2</sub>, a mass flow meter (MFM, Alicat Scientific) was used to measure the outlet gas stream from the cathode prior to sampling to the GC loop.<sup>34</sup> The FE for gaseous products was calculated using the following equation:

$$FE (\%) = \frac{zFxV}{j_{\text{total}}} \times 100\%$$

where *z* is the number of electrons transferred for producing a target product; *F* is the Faraday constant; *x* is the molar fraction of a target product determined by GC; *V* is the molar flow rate of gas; and *j<sub>total</sub>* is the total current density.

The liquid products after electrolysis were collected and quantified via <sup>1</sup>H nuclear magnetic resonance (NMR) spectroscopy using a Bruker NEO 400 MHz spectrometer. The electrolyte (500 µL) was mixed with an internal standard (100 µL of 5 mM 3-(trimethylsilyl)propionic-2,2,3,3-d<sub>4</sub> acid sodium salt in D<sub>2</sub>O). The partial current densities of CO and H<sub>2</sub> (*j<sub>CO</sub>* and *j<sub>H2</sub>*) at different cell voltages were determined by multiplying the overall current density by the corresponding FE. The single-pass CO<sub>2</sub> conversion efficiency (SPCE) is calculated as follows:

$$SPCE = \frac{\frac{j_{CO}}{zF} \times \frac{RT}{P}}{CO_2 \text{ flow rate}}$$

where *R* is the gas constant, *T* is the reaction temperature, and *P* is the reaction pressure.

## 3. Results and discussion

### 3.1. Pressurized electrolysis of CO<sub>2</sub> to CO

We systematically examined the effects of CO<sub>2</sub> partial pressure on the performance of an Ag GDE for the CO<sub>2</sub>RR over a pressure range of 1 to 10 bar. Fig. 1 illustrates the influence of pressure on FE<sub>CO</sub> and cell voltage under galvanostatic conditions at various temperatures of 20 °C, 40 °C, 60 °C, and 80 °C. We note that only CO and H<sub>2</sub> were detected across all experiments, with no liquid products that were observed or under the detection limit. Under ambient pressure and temperature (Fig. 1a), FE<sub>CO</sub> reached 95% at 100 mA cm<sup>-2</sup>, demonstrating the superior capability of Ag catalyst in converting CO<sub>2</sub> to CO. However, FE<sub>CO</sub> sharply declined to below 40% as the current density increased to 600 mA cm<sup>-2</sup>. This trend highlights a key challenge in MEA cells with AEM: high current densities drive substantial electroosmotic water flow accompanied by cation migration from the anode, resulting in electrode flooding and thickened CO<sub>2</sub> diffusion layer. The reduced flux of CO<sub>2</sub> near the catalyst surface leads to HER dominance.

Meanwhile, the elevated CO<sub>2</sub> consumption rate at higher current densities exacerbates mass transport limitations, hindering conversion efficiency. To substantiate this claim, we evaluated the CO<sub>2</sub> single pass conversion efficiency (SPCE) under varying current densities at 1 bar and 10 bar CO<sub>2</sub> pressures. As shown in Fig. S4 (ESI<sup>†</sup>), under 1 bar CO<sub>2</sub>, the SPCE initially increases with current density but plateaus at ~400 mA cm<sup>-2</sup>, indicating mass transport constraints. In contrast, at 10 bar CO<sub>2</sub>, the SPCE continues to rise, reaching a maximum at ~800 mA cm<sup>-2</sup>. These observations confirm that rapid CO<sub>2</sub> consumption at high current densities intensifies mass transport limitations, particularly under low CO<sub>2</sub> partial pressures.

By increasing the CO<sub>2</sub> pressure up to 10 bar, we effectively mitigate these limitations, resulting in higher FE<sub>CO</sub> at elevated current densities. Specifically, under 10 bar and 20 °C, FE<sub>CO</sub> remained above 95% even at 600 mA cm<sup>-2</sup>. This trend was also observed at higher temperature conditions (Fig. 1b-d). FE<sub>CO</sub> consistently increased with pressure under the current density,



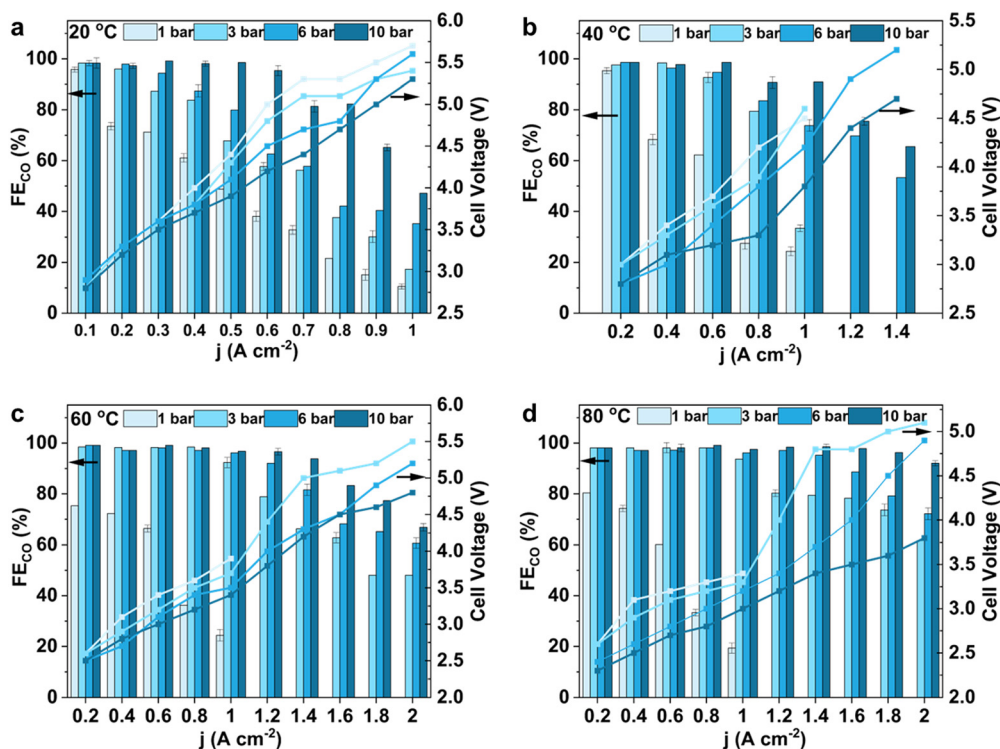


**Fig. 1**  $FE_{CO}$  and cell voltage as a function of current density for the CO<sub>2</sub>RR at various pressures (1 bar, 3 bar, 6 bar, and 10 bar) and temperatures: (a) 20 °C, (b) 40 °C, (c) 60 °C, and (d) 80 °C. A consistent input flow of 250 sccm CO<sub>2</sub> was employed in all experiments. The cathode was Ag GDE and the anode was Ir/Ti felt. 0.1 M KHCO<sub>3</sub> was used as an anolyte. The error bars represent standard deviations of three independent measurements.

signaling the effectiveness of pressurized conditions for the CO<sub>2</sub>RR to CO production.

The enhancement of  $FE_{CO}$  at high  $j$  with increasing pressure is associated with multiple factors: (i) Henry's law predicts that elevated CO<sub>2</sub> pressure increases the dissolved CO<sub>2</sub> concentration,<sup>35</sup> boosting CO<sub>2</sub> availability in the wetted catalyst layer as well as reducing proton adsorption, thereby effectively suppressing the HER; (ii) elevated pressure reduces the density difference between gas and liquid phases, thereby mitigating water flooding under high current densities.<sup>36</sup>

Encouragingly, elevated pressures across all temperatures consistently led to reductions in cell voltage, as shown in Fig. 1. At relatively lower current density, the drop is insignificant, as shown in Fig. 1(a), from 100 mA cm<sup>-2</sup> to 300 mA cm<sup>-2</sup> and the cell voltage variation is within 0.1 V from 1 bar to 10 bar. However, at higher current densities, the decrease of cell voltage with increasing pressure becomes particularly evident. For instance, at 80 °C under a current density of 1.8 A cm<sup>-2</sup>, increasing the pressure from 3 bar to 10 bar lowers the cell voltage from 5 V to 3.6 V. Calculations of thermodynamic potential across the studied range of pressure and temperature indicate minimal variation (~0.1 V; see Fig. S5 and S6, ESI<sup>†</sup>) for both the CO<sub>2</sub>RR and OER. Considering that under high current density, the fast CO<sub>2</sub> consumption rate leads to severe mass transfer limitation, we assume that the cell voltage reductions with increasing pressure are primarily due to decreased mass transfer resistance.

### 3.2. Effect of elevated temperature on CO<sub>2</sub>-to-CO conversion

Increasing the temperature also effectively reduces the overall cell voltage across all CO<sub>2</sub> pressures under a current density range of 0.1 to 2 A cm<sup>-2</sup> (Fig. S7, ESI<sup>†</sup>), consistent with previous high temperature MEA studies. The AEM shows negligible increase of ionic conductivity by 10 mS cm<sup>-1</sup> from 20 to 80 °C at 1 bar,<sup>30,37,38</sup> corresponding to an ohmic potential drop of around 0.20 V at 1 A cm<sup>-2</sup>, much lower than the cell voltage drop by 2.3 V. Considering the minimal thermodynamic potential variations for the pressure and temperature range under investigation (Fig. S5 and S6, ESI<sup>†</sup>), we posited that the reduction in cell voltage mainly arises from diminished kinetic overpotentials.

Fig. 2(a–c) illustrates the trend of  $FE_{CO}$  and  $j_{CO}$  as temperature increases under different CO<sub>2</sub> pressures (0.1 bar to 10 bar) and different applied cell voltages of 3 V, 3.4 V, and 3.8 V. At ambient CO<sub>2</sub> pressure (1 bar),  $FE_{CO}$  and  $j_{CO}$  exhibit a distinct temperature-dependent response related to cell voltage. Specifically, at a lower cell voltage of 3 V,  $FE_{CO}$  initially increased slightly as temperature rose from 20 to 40 °C before decreasing beyond 60 °C. Conversely, at higher cell voltages (3.4 V and 3.8 V), a progressive decline in  $FE_{CO}$  was observed with increasing temperature from 20 to 80 °C, with the rate of decrease becoming more pronounced at higher cell voltage. Regarding  $j_{CO}$ , at 3 V, a positive correlation with temperature was observed from 20 °C to 80 °C. However, at elevated cell voltages,  $j_{CO}$  followed a volcano-shaped trend, peaking at 60 °C for 3.4 V and

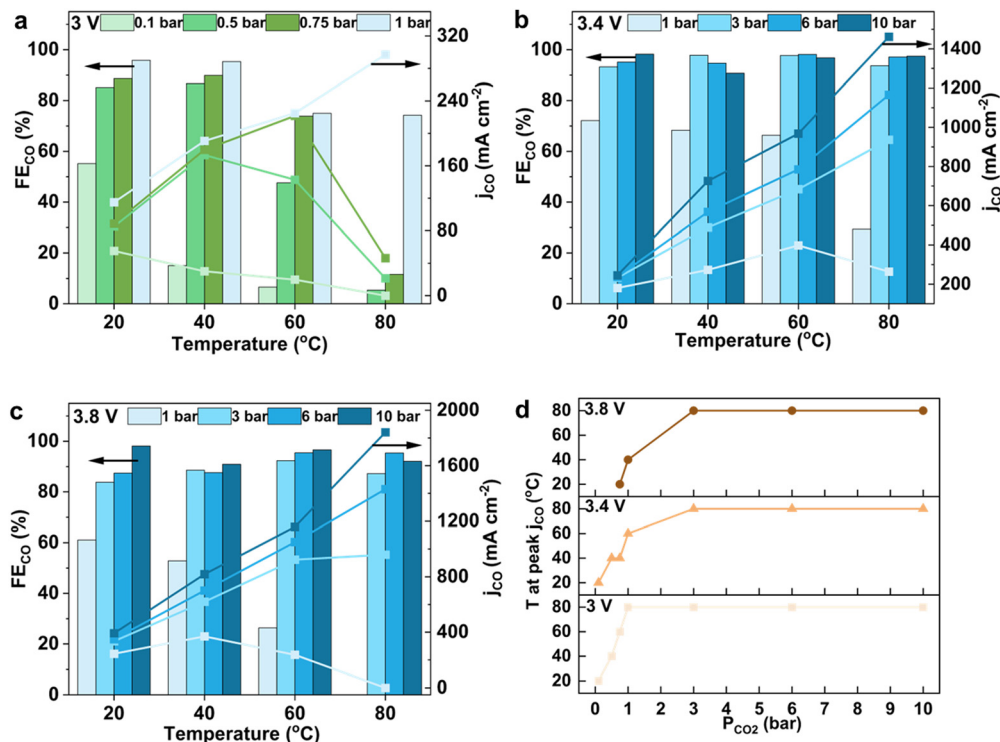


**Fig. 2** Effect of reaction temperature on the CO<sub>2</sub>RR performance. (a–c) FE<sub>CO</sub> and  $j_{CO}$  as a function of temperature at various CO<sub>2</sub> pressures for applied cell voltages of (a) 3 V, (b) 3.4 V, and (c) 3.8 V, (d) temperature for peak  $j_{CO}$  as a function of CO<sub>2</sub> pressure under different cell voltages. For the diluted CO<sub>2</sub>RR (0.1 bar to 0.75 bar) in (a), a CO<sub>2</sub>/N<sub>2</sub> gas mixture was fed with a total mass flow rate of 250 sccm. For the CO<sub>2</sub>RR under 1 bar and above in (b) and (c), dry pure CO<sub>2</sub> gas was supplied to the cathode at a flow rate of 250 sccm.

at 40 °C for 3.8 V, indicating that excessive heating suppresses CO production at higher cell voltages.

Temperature influences not only the intrinsic reaction kinetics of the CO<sub>2</sub>RR but also other critical parameters, such as CO<sub>2</sub> solubility and diffusion coefficients.<sup>39</sup> With increasing temperature, the diffusion coefficient of CO<sub>2</sub> in water rises (Fig. S8, ESI†), potentially enhancing mass transport. However, CO<sub>2</sub> solubility within the wet catalyst layer decreases (Fig. S9, ESI†), which could limit CO<sub>2</sub> availability at the catalyst surface. The interplay of these factors can be described by the diffusion-limited current density equation:

$$j = nF \frac{D \cdot C}{\delta}$$

where  $j$  is the limiting current density,  $n$  is number of electrons transferred per mole of reactant ( $n = 2$  for CO<sub>2</sub> reduction to CO),  $D$  is the diffusion coefficient of CO<sub>2</sub> in the electrolyte,  $C$  is the concentration (or solubility) of CO<sub>2</sub>, and  $\delta$  is the effective diffusion layer.

As demonstrated in Fig. S8 and S9 (ESI†), increasing the temperature from 20 °C to 80 °C results in a 3-fold decrease in CO<sub>2</sub> solubility, but a concurrent ~3-fold increase in its diffusivity. Intuitively, this would suggest a neutral net effect on  $j_{CO}$  if only  $D$  and  $C$  were to be considered. The decrease of  $j_{CO}$  with increasing temperature is linked to the improved surface wettability. Elevated temperatures also reduce the contact angle of water on the cathode surface, from 137° at 20 °C to 122° at 80 °C

(Fig. S10, ESI†). Enhanced wettability increases the effective diffusion layer ( $\delta$ ), imposes an additional mass transport barrier for CO<sub>2</sub>.

At lower cell voltages (e.g., 3.0 V), CO<sub>2</sub> consumption rates are modest, and the available CO<sub>2</sub> concentration remains in excess across the studied temperature range. Under these conditions, mass transport limitations are minimal, and  $j_{CO}$  benefits from enhanced intrinsic reaction kinetics as temperature rises under 1 bar CO<sub>2</sub> (Fig. 2a). In contrast, at higher cell voltages (e.g., 3.4 V and 3.8 V), CO<sub>2</sub> consumption rates rise substantially, and mass transport limitations become a dominant factor. As temperature increases, the combined effects of reduced CO<sub>2</sub> solubility and increased diffusion layer limit CO<sub>2</sub> flux to the catalyst surface. This results in a decline in  $j_{CO}$  with increasing temperature under ambient pressure (Fig. 2b and c).

While  $\delta$ ,  $D$ , and CO<sub>2</sub> solubility are all sensitive to temperature, CO<sub>2</sub> solubility is also tunable by pressure. Elevating the CO<sub>2</sub> pressure above 1 bar significantly increases solubility, thereby improving CO<sub>2</sub> flux and enabling a linear increase in  $j_{CO}$  as temperature rises (Fig. 2b and c). This synergy between high pressure and high temperature effectively overcomes the limitations imposed by mass transport and enhances overall CO<sub>2</sub>RR performance. Conversely, reducing the operating pressure below 1 bar shifts the temperature for peak  $j_{CO}$  to lower values (Fig. 2d), as the system becomes increasingly constrained by limited CO<sub>2</sub> solubility.

The temperature-dependent performance of  $\text{CO}_2$  reduction at varying cell voltages is closely linked to the shift in the reaction order of  $\text{CO}_2$ . As shown in Fig. 3a, at 3 V, the reaction order approaches zero from a pressure range of 0.75 bar to 10 bar, indicating sufficient  $\text{CO}_2$  availability to drive the reduction process. In contrast, at 3.4 V and 3.8 V, the reaction order increases to 0.15 and 0.3, respectively. At higher cell voltages, increased adsorption free energy of  $\text{CO}_2$ , as well as the rising surface coverage of adsorbed hydrogen ( $\theta_{\text{H}_{\text{ad}}}$ ), which introduces repulsive effects on the adsorbed carboxyl intermediate ( $\theta_{\text{COOH}_{\text{ad}}}$ ), improve the reliance on  $\text{CO}_2$  availability.<sup>41,42</sup>

To elucidate the temperature dependence of product selectivity in the  $\text{CO}_2\text{RR}$ ,  $j_{\text{CO}}$  and  $j_{\text{H}_2}$  were analyzed as a function of reciprocal temperature. Here we define the electrochemical driving energy ( $E_{\text{d}}$ ) using the following relationship:<sup>43</sup>

$$\ln(j) = -\frac{E_{\text{d}}}{R} \left( \frac{1}{T} \right) + \ln(A) \quad (1)$$

$$E_{\text{d}} = E_{\text{a}} - \alpha F \eta \quad (2)$$

where  $E_{\text{a}}$  is the activation energy,  $A$  is the pre-exponential factor,  $\alpha$  is charge transfer coefficient, and  $\eta$  is the overpotential. As illustrated in Fig. 3(b and c), Ag exhibits a notably lower  $E_{\text{d}}$  for CO formation ( $17.97 \text{ kJ mol}^{-1}$ ) compared to that for  $\text{H}_2$  ( $49.38 \text{ kJ mol}^{-1}$ ) at 3 V under 1 bar, underscoring the inherent capability of Ag to suppress the HER in favor of CO production under  $\text{CO}_2\text{RR}$  conditions. In addition, this difference of  $E_{\text{d}}$  suggests that the HER is significantly more sensitive to temperature variations than CO formation, benefiting more from elevated temperatures. As a result, at a  $\text{CO}_2$  pressure of 1 bar, while the temperature dependence of  $j_{\text{CO}}$  varies with applied cell voltages,  $j_{\text{H}_2}$  consistently increases with temperature across all cell voltages (Fig. S11, ESI†). As expected, both  $E_{\text{d}}$  values for  $\text{CO}_2$ -to-CO conversion and the HER exhibit a decreasing trend with increasing cell voltage. Meanwhile, as the pressure further increased to 10 bar, we found a rising trend of  $E_{\text{d}}$  of the  $\text{CO}_2\text{RR}$  but a decreasing trend of  $E_{\text{d}}$  of the HER (Fig. S12, ESI†), which might be related to the change of  $\alpha$  under different pressures.

### 3.3. Synergy of pressure and temperature effects

Temperature and pressure were found to have synergistic effects on  $\text{CO}_2\text{RR}$  performance. The  $\text{CO}_2$  availability plays a crucial role in modulating the temperature effect on  $\text{CO}_2\text{RR}$  performance, including the  $\text{FE}_{\text{CO}}$  and  $j_{\text{CO}}$ . Under a constant current density for the  $\text{CO}_2\text{RR}$ , at a pressure of 1 bar, increasing the temperature from 20 to 40 °C slightly enhances the  $\text{FE}_{\text{CO}}$  ranging from 100 to 1000 mA cm<sup>-2</sup> (Fig. S13, ESI†). Specifically, at 500 mA cm<sup>-2</sup>, increasing the temperature from 20 to 40 °C leads to the  $\text{FE}_{\text{CO}}$  increase from 48% to 64%. However, further increasing the temperature did not result in substantial improvements in  $\text{FE}_{\text{CO}}$ , with only a 10% variation (60 °C > 80 °C > 40 °C) in  $\text{FE}_{\text{CO}}$  observed. In contrast, at pressures exceeding 3 bar, the  $\text{FE}_{\text{CO}}$  value shows a gradual increase with rising temperatures from 20 to 80 °C, signaling that the impact of temperature on  $\text{FE}_{\text{CO}}$  under constant current density is more evident at higher pressures, particularly under high current densities. This trend underscores the critical interplay between pressure and temperature in enhancing  $\text{FE}_{\text{CO}}$  under constant current density. At higher pressures, the increased  $\text{CO}_2$  concentration around the catalyst layer counteracts the solubility limitation imposed by elevated temperatures, overcoming mass transfer limitations of reactants to sustain high reaction rates of the  $\text{CO}_2\text{RR}$ . Remarkably, as illustrated in Fig. 1d, at 80 °C, the  $\text{FE}_{\text{CO}}$  value increases from 19% at 1 bar to nearly 100% at 10 bar under a current density of 1 A cm<sup>-2</sup>, further maintaining a high  $\text{FE}_{\text{CO}}$  close to 95% from 1 A cm<sup>-2</sup> to 2 A cm<sup>-2</sup>.

Under constant cell voltage conditions for the  $\text{CO}_2\text{RR}$ , the intrinsic temperature-dependent increase in reaction rates drives simultaneous increases in  $j_{\text{CO}}$  and  $j_{\text{H}_2}$  at lower cell voltages where  $\text{CO}_2$  availability remains sufficient to sustain the  $\text{CO}_2\text{RR}$  despite diminished solubility at elevated temperatures (e.g., 80 °C) even under ambient pressure, demonstrating the positive kinetic effects of temperature. However, at higher cell voltages, where  $\text{CO}_2$  reliance and mass transfer limitations increase, the reduced  $\text{CO}_2$  solubility at elevated temperatures results in a decline in  $j_{\text{CO}}$ . Increasing  $\text{CO}_2$  availability through elevated  $\text{CO}_2$  pressure mitigates these limitations and allows for the full utilization of the temperature-dependent

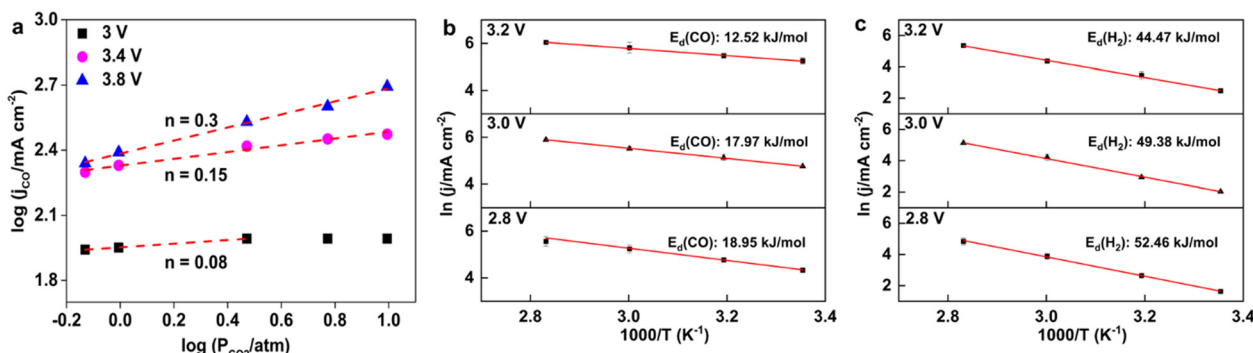


Fig. 3 (a) Reaction order for  $\text{CO}_2$  derived from the logarithmic dependence of  $j_{\text{CO}}$  on  $\text{CO}_2$  pressure at various applied cell voltages (3 V, 3.4 V, and 3.8 V) from a pressure range of 0.75 bar to 10 bar. (b)  $E_{\text{d}}$  for the  $\text{CO}_2\text{RR}$  to CO at 2.8 V, 3 V, and 3.2 V at 1 bar. (c)  $E_{\text{d}}$  for the HER at 2.8 V, 3 V, and 3.2 V at 1 bar. The error bars represent the standard deviations of three independent measurements.



enhancement of  $j_{CO}$ . As shown in Fig. 2(c), at an applied cell voltage of 3.8 V and a pressure of 3 bar,  $j_{CO}$  increases steadily with temperature up to 60 °C, although the rate of improvement diminishes at 80 °C. However, as long as the CO<sub>2</sub> pressure is sufficiently high (above 6 bar), the positive temperature effects on  $j_{CO}$  still consistently outweigh the adverse impact of reduced CO<sub>2</sub> solubility, enabling sustained increases in  $j_{CO}$  with temperature. Additionally, we observed that elevated pressure effectively constrains the increase in  $j_{H_2}$  with temperature (Fig. S11, ESI†), further underscoring the efficacy of high-pressure operations at high temperatures to constrain the HER.

To further validate the critical role of CO<sub>2</sub> availability in shaping the temperature dependence of CO<sub>2</sub>RR performance, we explored CO<sub>2</sub>RR performance under diluted CO<sub>2</sub> conditions at varying temperatures. CO<sub>2</sub> was mixed with N<sub>2</sub> to get controlled concentrations of 10 vol%, 50 vol%, and 75 vol% (with a total flow rate of 250 sccm). As shown in Fig. 2a, at 3 V, both FE<sub>CO</sub> and  $j_{CO}$  declined sharply with increasing temperatures under extremely low CO<sub>2</sub> partial pressure (0.1 bar), where the positive kinetic effect of temperature on the CO<sub>2</sub>RR is entirely offset by reduced CO<sub>2</sub> solubility. In contrast, when CO<sub>2</sub> pressure exceeded 0.5 bar, FE<sub>CO</sub> shows a slight increase from 20 to 40 °C before declining significantly above 60 °C. Interestingly, with increasing CO<sub>2</sub> pressure, the peak temperature for  $j_{CO}$  gradually shifted to a higher position: 20 °C, 40 °C, 60 °C, and 80 °C for 0.1 bar, 0.5 bar, 0.75 bar, and 1 bar, respectively (Fig. 2d). It highlights that the temperature effect on  $j_{CO}$  is highly reliable on CO<sub>2</sub> pressure: as CO<sub>2</sub> partial pressure increases, the CO<sub>2</sub>RR could benefit more from temperature elevation. In addition, we investigated the effect of CO<sub>2</sub> supply rate on CO<sub>2</sub>RR performance by varying flow rates (10–250 sccm) under pure CO<sub>2</sub> conditions. The nearly constant FE<sub>CO</sub> across all flow rates at 20–80 °C suggests that reduced performance at low CO<sub>2</sub> partial pressure is due to decreased CO<sub>2</sub> concentration rather than the absolute CO<sub>2</sub> supply (Fig. S14, ESI†).

Although previous studies have explored the individual effects of elevated pressure and temperature on Ag-based catalysts for CO<sub>2</sub> reduction to CO, comprehensive investigations that systematically examine the combined influence of temperature, pressure, and cell voltage within MEA systems remain limited. In contrast, our study presents a holistic optimization

strategy, integrating temperature, pressure, and cell voltage control within an MEA system. Notably, we demonstrate a remarkable  $j_{CO}$  value of 1840 mA cm<sup>-2</sup> with an FE<sub>CO</sub> value of 92% at 10 bar and 80 °C. To the best of our knowledge, this represents one of the highest performances reported for the CO<sub>2</sub>RR to CO under industrially relevant conditions in an MEA configuration. This performance significantly surpasses previous reports that explored either elevated temperature or pressure independently (Fig. S16, ESI†).

Furthermore, while earlier studies have investigated pressurization in MEA cells, they typically applied pressure solely to the cathode compartment. Such asymmetric pressurization can result in significant pressure differentials across the membrane, leading to gas crossover, increased membrane degradation, and ultimately compromised system stability and performance. Our study, by contrast, adopts a balanced pressure strategy, applying equalized pressures to both the anode and cathode compartments. This approach mitigates pressure-driven membrane stress, eliminates crossover issues, and enables stable operation at high pressures, thereby advancing MEA durability and practical scalability.

To evaluate long-term operational stability, the pressurized CO<sub>2</sub> electrolyzer employing an Ag-based cathode was tested at 40 °C and 10 bar for over 100 hours at a constant current density of 300 mA cm<sup>-2</sup>. During earlier experiments, we found that the 20 µm AEM was prone to mechanical failure under combined high-temperature (>60 °C) and high-pressure (>6 bar) conditions. To address this, a thicker 40 µm AEM was employed for the stability test. While this modification improved mechanical robustness, it also led to higher cell voltages due to increased ohmic resistance.

As shown in Fig. 4, the FE<sub>CO</sub> remained above 95% for the first 83 hours, indicating highly stable performance. Beyond this point, a gradual decline in FE<sub>CO</sub> was observed. Notably, this drop in selectivity was not accompanied by a significant increase in the HER, and the total FE remained around 85% after 95 hours. We hypothesize that the decline in FE<sub>CO</sub> arises from increased gas permeability of the membrane. This is supported by the observed 10% reduction in the measured flow rate at the cathode outlet and the presence of gas bubbles on the anode side when the electrochemical reaction was paused.

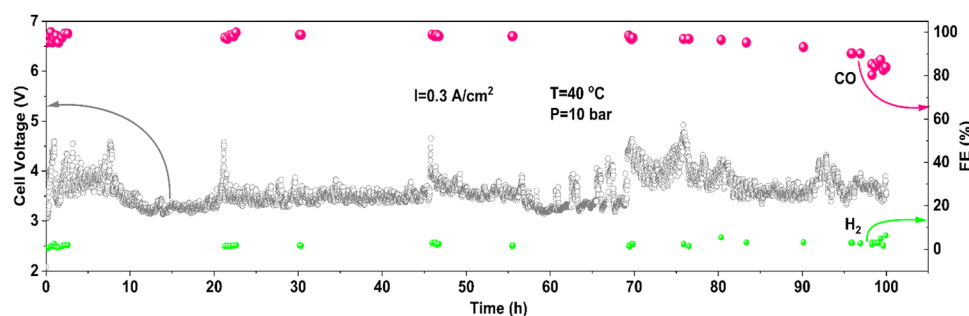


Fig. 4 Long-term stability test of the pressurized CO<sub>2</sub> electrolyzer using a Ag cathode at 40 °C and 10 bar with a constant current density of 300 mA cm<sup>-2</sup>. The cell voltage (left axis, grey) and FE<sub>CO</sub> (pink) and H<sub>2</sub> (green) (right axis) are shown over 100 hours of continuous operation. A 40 µm AEM was employed.



These signs suggest that prolonged exposure to elevated pressure and temperature may compromise membrane integrity. In additional tests conducted at 60 °C and 10 bar, membrane degradation occurred more rapidly, with total FE decreasing from nearly 100% to 60% within 30 hours, further highlighting the challenge of maintaining membrane stability under desired temperature and pressure conditions.

### 3.4. Pure-water-fed electrolysis under high pressure and temperature

To reduce the cell voltage, we explored the use of 1 M KOH as the anolyte. Alkaline electrolytes like 1 M KOH offer reduced ohmic losses compared to 0.1 M  $\text{KHCO}_3$  due to their higher conductivity. As shown in Fig. 5a, substituting 1 M KOH for 0.1 M  $\text{KHCO}_3$  did not affect the  $\text{FE}_{\text{CO}}$ , which still reached 90% at  $2 \text{ A cm}^{-2}$  under 10 bar and 80 °C. Importantly, the cell voltage was further reduced to  $3.2 \text{ V}$  for  $2 \text{ A cm}^{-2}$  (Fig. S17, ESI<sup>†</sup>).

During experimentation, however, we observed that using 1 M KOH under 10 bar and 20 °C led to blockage of the cathode flow field due to salt precipitation within five minutes, causing the  $\text{CO}_2$  inlet pressure to rise over 1.4 bar. This effect is likely due to the increased  $\text{CO}_2$  concentration, which enhances the reaction between  $\text{CO}_2$  and cathodically generated  $\text{OH}^-$ , resulting in intense salt formation. The resulting salt precipitation obstructs the flow field and GDE, limiting  $\text{CO}_2$  mass transfer. Interestingly, when operating at an elevated temperature of 80 °C under the same 10 bar pressure, salt precipitation is significantly mitigated. Blockage only occurred after two hours of continuous operation, as indicated by a similar rise in  $\text{CO}_2$  inlet pressure beyond 1.4 bar. While some studies suggest that  $\text{K}_2\text{CO}_3$  is the dominant salt precipitating at the cathode and that  $\text{CO}_2$  crossover occurs primarily *via* carbonate ions rather than bicarbonate,<sup>23,44,45</sup> others observed the exclusive formation of  $\text{KHCO}_3$  at the cathode which has lower solubility than  $\text{K}_2\text{CO}_3$ .<sup>46</sup> Regardless of the specific salt species, elevated temperatures effectively increase the solubility of both  $\text{KHCO}_3$  and  $\text{K}_2\text{CO}_3$  (Fig. S18 and S19, ESI<sup>†</sup>), thereby reducing the extent of salt buildup and mitigating flow field obstruction.

Although elevated temperatures can mitigate salt accumulation, eventual blockage remains inevitable due to the crossover

of  $\text{K}^+$  ions, resulting in system instability over time.<sup>47</sup> Several strategies have been explored to address this issue. Acidic electrolytes, for example, allow bulk protons to react with carbonate, regenerating  $\text{CO}_2$  locally. However, acidic media require high concentrations of alkali metal cations to suppress the HER in the proton-rich environment.<sup>48–51</sup> Their continuous accumulation in the Helmholtz layer can eventually cause alkali metal salt crystallization on the catalyst and GDL.<sup>52</sup> Bipolar membrane (BPM) systems present an alternative strategy by creating an acidic cathode environment that eliminates carbonate formation. These systems regenerate  $\text{CO}_2$  through the reaction of carbonate or bicarbonate with protons, effectively addressing salt precipitation.<sup>53,54</sup> However, the acidic cathode environment promotes the HER, thus reducing  $\text{CO}_2\text{RR}$  selectivity, while BPM systems suffer from intrinsic drawbacks, including high resistance and long-term instability.

We employed a pure water feed (deionized water,  $17.8 \text{ M}\Omega \text{ cm}$ ) at the anode of the AEM-based MEA cell. No anion exchange ionomer was incorporated into the cathodic catalyst layer. However, the PiperION AEM used in this study is functionalized with highly stable piperidinium cations, which are embedded within a rigid, hydrophobic, ether-bond-free aryl backbone.<sup>55</sup> Recent studies suggest that organic cations, such as tetraalkylammonium species, could efficiently catalyze the  $\text{CO}_2\text{RR}$  by modulating the interfacial electric field, facilitating the activation of  $\text{CO}_2$  and stabilizing the transition state, improving both the rate and selectivity of the  $\text{CO}_2\text{RR}$ .<sup>56</sup> Similarly, the piperidinium cations in the PiperION AEM have been proposed to enhance  $\text{CO}_2\text{RR}$  performance *via* a comparable mechanism, despite the absence of alkali metal cations in the cathode compartment.

Under ambient conditions, the HER was the dominant reaction.  $\text{FE}_{\text{CO}}$  was below 30% at  $100 \text{ mA cm}^{-2}$ , further dropping to less than 10% at  $500 \text{ mA cm}^{-2}$  (Fig. 5b). In stark contrast, under 10 bar and 80 °C,  $\text{FE}_{\text{CO}}$  reached nearly 100% at  $100 \text{ mA cm}^{-2}$  and  $200 \text{ mA cm}^{-2}$ , with a slight reduction to 90% at  $300 \text{ mA cm}^{-2}$ . In addition, the cell voltage decreased dramatically under high-pressure and high-temperature conditions. For example, at  $300 \text{ mA cm}^{-2}$ , the cell voltage dropped from  $5.3 \text{ V}$  at ambient conditions to  $3.6 \text{ V}$  under 10 bar and 80 °C.

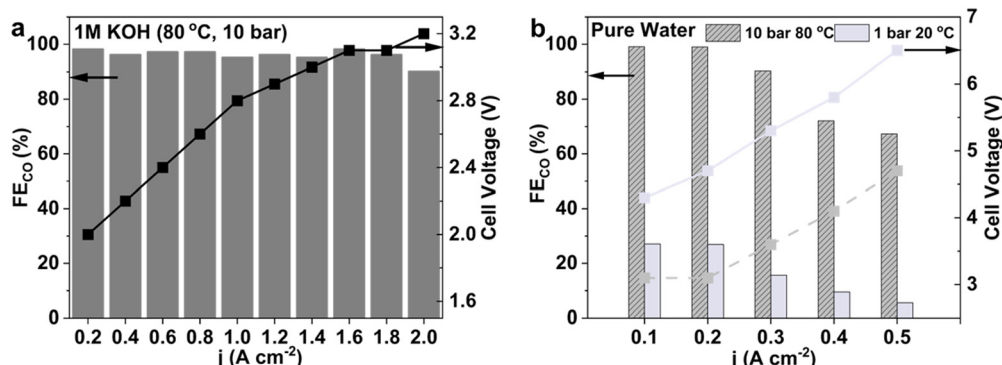


Fig. 5 (a)  $\text{FE}_{\text{CO}}$  and cell voltage as a function of current density for the  $\text{CO}_2\text{RR}$  in 1 M KOH anolyte at 80 °C and 10 bar. (b) Comparison of  $\text{FE}_{\text{CO}}$  and cell voltage at varying current densities for the pure-water-fed  $\text{CO}_2\text{RR}$  at 10 bar and 80 °C versus ambient conditions (1 bar, 20 °C).



Compared to previous MEA studies employing pure water feeds to anode, our system exhibits comparatively lower performance.<sup>21,30</sup> Notably, Zhuang *et al.*<sup>30</sup> reported an impressive  $FE_{CO}$  value exceeding 85% at 60 °C and 1 bar, achieving current densities as high as 500 mA cm<sup>-2</sup>. Our system achieved 65%  $FE_{CO}$  at 500 mA cm<sup>-2</sup> at 10 bar and 80 °C. This performance difference likely arises from variations in the membrane composition and the use of ionomers with smaller organic cations, known to strengthen interfacial electric fields and enhance CO<sub>2</sub> activation kinetics.<sup>57</sup> Nevertheless, our findings uniquely highlight that increasing CO<sub>2</sub> pressure markedly improves CO<sub>2</sub>RR efficiency beyond ambient limitations, thus presenting a promising strategy for optimizing electrochemical CO<sub>2</sub> conversion under H<sub>2</sub>O feedstock.

### 3.5. CO<sub>2</sub>RR using dilute CO<sub>2</sub> feedstock

Currently, CO<sub>2</sub> capture and reduction are typically conducted as separate processes, with the purification of CO<sub>2</sub> from flue gas contributing substantially to the overall cost of the CO<sub>2</sub> electrolysis system.<sup>58</sup> Industrial CO<sub>2</sub> capture technologies, such as those using monoethanolamine (MEOA), are estimated to cost at least \$44 per ton of CO<sub>2</sub> captured.<sup>59</sup> Direct utilization of low-concentration CO<sub>2</sub> (10 vol% balanced by N<sub>2</sub>), similar to real flue gas compositions,<sup>60</sup> as a feedstock for the CO<sub>2</sub>RR could drastically lower costs and enhance the overall efficiency of the process.<sup>61,62</sup> However, the low volume fraction of CO<sub>2</sub> in such streams limits the electroreduction process and exacerbates the

HER, particularly at high current densities where CO<sub>2</sub> consumption increases rapidly.<sup>63,64</sup>

We establish that our pressurized MEA configuration could significantly enhance the conversion of dilute CO<sub>2</sub> feedstocks. Electrolysis experiments were conducted using gas feeds where CO<sub>2</sub> was diluted with N<sub>2</sub>, with pressurization employed to elevate the partial pressure of CO<sub>2</sub>. Using a dilute CO<sub>2</sub> feed (10 vol%) at 1 bar resulted in consistently low  $FE_{CO}$  values across 100–500 mA cm<sup>-2</sup>, with nearly zero  $FE_{CO}$  values beyond 400 mA<sup>-2</sup> (Fig. 6a). However, when 10 vol% CO<sub>2</sub> feed was pressurized to 10 bar, there was a notable enhancement in  $FE_{CO}$ , similar to that of pure CO<sub>2</sub> feeds, demonstrating that elevated pressure effectively increases CO<sub>2</sub> availability at the catalyst surface and overcomes the mass transfer limitations under the diluted CO<sub>2</sub>RR. Notably, pressurized (10 bar) CO<sub>2</sub>RR with 10 vol% CO<sub>2</sub> demonstrated performance comparable to, or slightly exceeding, that of 1 bar CO<sub>2</sub>RR with 100% CO<sub>2</sub> (Fig. 6a).

Additionally, we observed that for the 10 vol% CO<sub>2</sub>RR at 1 bar, elevated temperatures adversely affected  $FE_{CO}$  (Fig. 6b and c). However, for the 10 vol% CO<sub>2</sub>RR at 10 bar, increasing temperature had a minimal effect on  $FE_{CO}$  at a current density of 100 mA cm<sup>-2</sup>, while dramatically reducing the cell voltage by 0.7 V from 20 to 80 °C (Fig. 6b and Fig. S20, ESI<sup>†</sup>). At higher current densities (200–500 mA cm<sup>-2</sup>), an operational temperature of 60 °C yielded the maximum  $FE_{CO}$ . Further increasing the temperature to 80 °C resulted in a decline of performance,

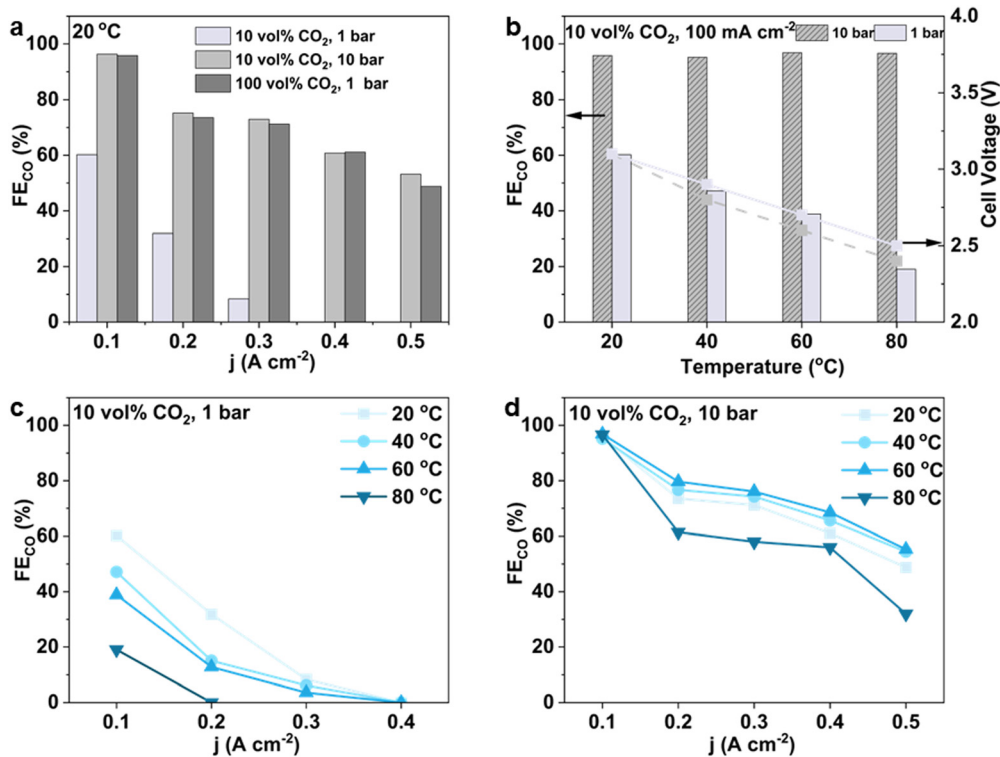


Fig. 6 (a)  $FE_{CO}$  as a function of current density under different CO<sub>2</sub> concentrations (10 vol% and 100 vol%) and reaction pressures (1 bar and 10 bar) at 20 °C. (b)  $FE_{CO}$  and cell voltage as functions of temperature for the CO<sub>2</sub>RR at 100 mA cm<sup>-2</sup> for 10 vol% CO<sub>2</sub> and reaction pressure of 1 bar and 10 bar. (c) and (d)  $FE_{CO}$  at different temperatures (20 °C, 40 °C, 60 °C, and 80 °C) for 10 vol% CO<sub>2</sub> and reaction pressure of (c) 1 bar and (d) 10 bar.



as the decreased  $\text{CO}_2$  solubility at this elevated temperature offsets the kinetic benefits gained from temperature increase.

Techno-economic analysis (see Supplementary Notes, ESI<sup>†</sup>) reveals that operating under elevated pressure introduces only a modest increase in dedicated capital and operating costs. In contrast, the enhanced reaction rate at higher current densities substantially reduces the required electrolyzer area, resulting in a net reduction in system-scale cost. For pure  $\text{CO}_2$  feedstock, this corresponds to a ~90% reduction in electrolyzer capital cost compared to operation under ambient conditions. Furthermore, for low-purity feedstocks (e.g., 10%  $\text{CO}_2$  in simulated flue gas), the cost of direct pressurization to 10 bar is estimated at US\$ 23 per ton of  $\text{CO}_2$  equivalent, which is nearly 80% lower than the cost of conventional  $\text{CO}_2$  capture technologies (~US\$ 100 per ton  $\text{CO}_2$ ).<sup>65</sup>

## 4. Conclusions

In summary, this study demonstrates that the combined effects of elevated temperature and pressure significantly enhance  $\text{CO}_2$  electrolysis to CO at industrially relevant current densities in a MEA electrolyzer employing commercial Ag nanoparticles. Pressurized  $\text{CO}_2$  not only increases the  $\text{CO}_2$  concentration at the catalyst surface, thereby suppressing the competing HER at ambient temperatures, but also sustains high  $\text{CO}_2$  reduction rates at elevated temperatures by counteracting the reduced  $\text{CO}_2$  solubility and enhanced wetting of catalyst layer caused by rising temperatures. This unique synergy of high temperature and pressure boosts CO current density to  $2 \text{ A cm}^{-2}$  with exceptional  $\text{FE}_{\text{CO}}$  (>90%) values under 80 °C and 10 bar. This is because increased thermal energy accelerates reaction kinetics while sufficient  $\text{CO}_2$  availability by high pressure mitigates mass transport limitations. Meanwhile, elevated temperature and pressure effectively lowers the cell voltage by reducing the mass transfer and kinetic overpotentials. Additionally, the pressurized MEA cell exhibits stable CO production, achieving  $\text{FE}_{\text{CO}} > 90\%$  at  $300 \text{ mA cm}^{-2}$  and a cell voltage of 3.6 V under 80 °C and 10 bar, even using pure water as the anolyte. Moreover, under dilute  $\text{CO}_2$  feed conditions (10 vol%  $\text{CO}_2$ ), the system achieves an  $\text{FE}_{\text{CO}}$  of 96% at  $100 \text{ mA cm}^{-2}$ , under 10 bar and ambient temperature. Increasing the temperature to 80 °C maintains the  $\text{FE}_{\text{CO}}$  while dramatically reducing the cell voltage by 0.7 V. Given that the operational conditions of commercial  $\text{CO}_2$  electroreduction systems are expected to function at elevated temperatures and pressures, these findings present a scalable pathway for  $\text{CO}_2$  electrolyzers to meet the demands of industrial applications.

## Author contributions

J. W. conceptualized and led the project, supervised the research activities, and provided critical revisions to the manuscript. Y. L. performed the experiments, analyzed the data, and drafted the manuscript. H. L. and R. J. contributed to the

construction of the experimental setup. M. P. helped with characterization.

## Data availability

All data supporting the findings of this study are included within the article and its ESI.<sup>†</sup> Any additional information related to the data is available upon request from the corresponding author.

## Conflicts of interest

The authors declare no competing financial interest.

## Acknowledgements

This research was financially supported by the Office of Research at the University of Cincinnati.

## References

- 1 A. Rode, T. Carleton, M. Delgado, M. Greenstone, T. Houser, S. Hsiang, A. Hultgren, A. Jina, R. E. Kopp, K. E. McCusker, I. Nath, J. Rising and J. Yuan, Estimating a Social Cost of Carbon for Global Energy Consumption, *Nature*, 2021, **598**(7880), 308–314.
- 2 B. Tang and F. Xiao, An Overview of Solar-Driven Photoelectrochemical  $\text{CO}_2$  Conversion to Chemical Fuels, *ACS Catal.*, 2022, **12**(15), 9023–9057.
- 3 Q. Cheng, M. Huang, L. Xiao, S. Mou, X. Zhao, Y. Xie, G. Jiang, X. Jiang and F. Dong, Unraveling the Influence of Oxygen Vacancy Concentration on Electrocatalytic  $\text{CO}_2$  Reduction to Formate over Indium Oxide Catalysts, *ACS Catal.*, 2023, **13**(6), 4021–4029.
- 4 P. Li, J. Liu, Y. Wang, X. Zhang, Y. Hou, Y. Zhang, X. Sun, X. Kang, Q. Zhu and B. Han, Manipulation of Oxygen Species on an Antimony-Modified Copper Surface to Tune the Product Selectivity in  $\text{CO}_2$  Electroreduction, *J. Am. Chem. Soc.*, 2024, **146**(38), 26525–26533.
- 5 J. Jin, J. Wicks, Q. Min, J. Li, Y. Hu, J. Ma, Y. Wang, Z. Jiang, Y. Xu, R. Lu, G. Si, P. Papangelakis, M. Shakouri, Q. Xiao, P. Ou, X. Wang, Z. Chen, W. Zhang, K. Yu, J. Song, J. Jiang, P. Qiu, Y. Lou, D. Wu, Y. Mao, A. Ozden, C. Wang, B. Y. Xia, X. Hu, V. P. Dravid, Y. M. Yiu, T. K. Sham, Z. Wang, D. Sinton, L. Mai, E. H. Sargent and Y. Pang, Constrained  $\text{C}_2$  Adsorbate Orientation Enables CO-to-Acetate Electroreduction, *Nature*, 2023, **617**(7962), 724–729.
- 6 H. Deng, T. Liu, W. Zhao, J. Wang, Y. Zhang, S. Zhang, Y. Yang, C. Yang, W. Teng, Z. Chen, G. Zheng, F. Li, Y. Su, J. Hui and Y. Wang, Substituent Tuning of Cu Coordination Polymers Enables Carbon-Efficient  $\text{CO}_2$  Electroreduction to Multi-Carbon Products, *Nat. Commun.*, 2024, **15**(1), 1–12.
- 7 S. Verma, B. Kim, H.-R. Jhong, S. Ma and P. J. A. Kenis, A Gross-Margin Model for Defining Technoeconomic



Benchmarks in the Electroreduction of CO<sub>2</sub>, *ChemSusChem*, 2016, **9**(15), 1972–1979.

8 A. Reyes, R. P. Jansonius, B. A. W. Mowbray, Y. Cao, D. G. Wheeler, J. Chau, D. J. Dvorak and C. P. Berlinguette, Managing Hydration at the Cathode Enables Efficient CO<sub>2</sub> Electrolysis at Commercially Relevant Current Densities, *ACS Energy Lett.*, 2020, **5**(5), 1612–1618.

9 D. Kopljarić, A. Inan, P. Vindayer, N. Wagner and E. Klemm, Electrochemical Reduction of CO<sub>2</sub> to Formate at High Current Density Using Gas Diffusion Electrodes, *J. Appl. Electrochem.*, 2014, **44**(10), 1107–1116.

10 S. Ma, M. Sadakiyo, R. Luo, M. Heima, M. Yamauchi and P. J. Kenis, One-Step Electrosynthesis of Ethylene and Ethanol from CO<sub>2</sub> in an Alkaline Electrolyzer, *J. Power Sources*, 2015, **301**, 219–228.

11 H. Rabiee, L. Ge, X. Zhang, S. Hu, M. Li and Z. Yuan, Gas Diffusion Electrodes (GDEs) for Electrochemical Reduction of Carbon Dioxide, Carbon Monoxide, and Dinitrogen to Value-Added Products: A Review, *Energy Environ. Sci.*, 2021, **14**(4), 1959–2008.

12 E. W. Lees, B. A. W. Mowbray, F. G. L. Parlante and C. P. Berlinguette, Gas Diffusion Electrodes and Membranes for CO<sub>2</sub> Reduction Electrolyzers, *Nat. Rev. Mater.*, 2021, **7**(1), 55–64.

13 D. Wakerley, S. Lamaison, J. Wicks, A. Clemens, J. Feaster, D. Corral, S. A. Jaffer, A. Sarkar, M. Fontecave, E. B. Duoss, S. Baker, E. H. Sargent, T. F. Jaramillo and C. Hahn, Gas Diffusion Electrodes, Reactor Designs, and Key Metrics of Low-Temperature CO<sub>2</sub> Electrolyzers, *Nat. Energy*, 2022, **7**(2), 130–143.

14 D. A. Salvatore, C. M. Gabardo, A. Reyes, C. P. O'Brien, S. Holdcroft, P. Pintauro, B. Bahar, M. Hickner, C. Bae, D. Sinton, E. H. Sargent and C. P. Berlinguette, Designing Anion Exchange Membranes for CO<sub>2</sub> Electrolyzers, *Nat. Energy*, 2021, **6**(4), 339–348.

15 Z. Xing, L. Hu, D. S. Ripatti and X. Feng, Enhancing Carbon Dioxide Gas-Diffusion Electrolysis by Creating a Hydrophobic Catalyst Microenvironment, *Nat. Commun.*, 2021, **12**(1), 136.

16 L. Weng, A. T. Bell and A. Z. Weber, Modeling Gas-Diffusion Electrodes for CO<sub>2</sub> Reduction, *Phys. Chem. Chem. Phys.*, 2018, **20**(25), 16973–16984.

17 T. Burdyny and W. A. Smith, CO<sub>2</sub> Reduction on Gas-Diffusion Electrodes and Why Catalytic Performance Must Be Assessed at Commercially Relevant Conditions, *Energy Environ. Sci.*, 2019, **12**(5), 1442–1453.

18 Z. Xing, X. Hu and X. Feng, Tuning the Microenvironment in Gas-Diffusion Electrodes Enables High-Rate CO<sub>2</sub> Electrolysis to Formate, *ACS Energy Lett.*, 2021, **6**(5), 1694–1702.

19 Y. Sun, J. Chen, X. Du, J. Cui, X. Chen, C. Wu, X. Yang, L. Liu and J. Ye, Anchoring Cs<sup>+</sup> Ions on Carbon Vacancies for Selective CO<sub>2</sub> Electroreduction to CO at High Current Densities in Membrane Electrode Assembly Electrolyzers, *Angew. Chem. Int. Ed.*, 2024, **63**, e202410802.

20 C. Lim, S. Kim, J. H. Song, M. H. Han, Y. Ko, K. Lee, J. Choi, W. H. Lee and H. Oh, Breaking the Current Limitation of Electrochemical CO<sub>2</sub> Reduction via a Silica-Hydroxide Cycle, *Energy Environ. Sci.*, 2024, **17**(17), 6215–6224.

21 M. Heßelmann, J. K. Lee, S. Chae, A. Tricker, R. G. Keller, M. Wessling, J. Su, D. Kushner, A. Z. Weber and X. Peng, Pure-Water-Fed Forward-Bias Bipolar Membrane CO<sub>2</sub> Electrolyzer, *ACS Appl. Mater. Interfaces*, 2024, **16**(19), 24649–24659.

22 J. Park, E. Kim, S. Kim, C. Lim, H. Kim, Y. Ko, J. Choi, H. Oh and W. H. Lee, Deriving an Efficient and Stable Microenvironment for a CO<sub>2</sub> MEA Electrolyzer by Reverse Osmosis, *ACS Energy Lett.*, 2024, **9**(7), 3342–3350.

23 B. Endrődi, E. Kecsenovity, A. Samu, F. Darvas, R. V. Jones, V. Török, A. Danyi and C. Janáky, Multilayer Electrolyzer Stack Converts Carbon Dioxide to Gas Products at High Pressure with High Efficiency, *ACS Energy Lett.*, 2019, **4**(7), 1770–1777.

24 B. Yang, K. Liu, H. J. W. Li, C. Liu, J. Fu, H. Li, E. J. Huang, P. Ou, T. Alkayyali, C. Cai, Y. Duan, H. Liu, P. An, N. Zhang, W. Li, X. Qiu, C. Jia, J. Hu, L. Chai, Z. Lin, Y. Gao, M. Miyauchi, E. Cortés, S. A. Maier and M. Liu, Accelerating CO<sub>2</sub> Electroreduction to Multicarbon Products via Synergistic Electric-Thermal Field on Copper Nanoneedles, *J. Am. Chem. Soc.*, 2024, **144**(7), 3039–3049.

25 W. Lee, Y. E. Kim, M. H. Youn, S. K. Jeong and K. T. Park, Catholyte-Free Electrocatalytic CO<sub>2</sub> Reduction to Formate, *Angew. Chem. Int. Ed.*, 2018, **57**(23), 6883–6887.

26 R. Küngas, Review—Electrochemical CO<sub>2</sub> Reduction for CO Production: Comparison of Low- and High-Temperature Electrolysis Technologies, *J. Electrochem. Soc.*, 2020, **167**(4), 044508.

27 D. Aaron and C. Tsouris, Separation of CO<sub>2</sub> from Flue Gas: A Review, *Sep. Sci. Technol.*, 2005, **40**(1–3), 321–348.

28 S. Piontek, C. Andronescu, A. Zaichenko, B. Konkena, K. J. Puring, B. Marler, H. Antoni, I. Sinev, M. Muhler, D. Mollenhauer, B. R. Cuenya, W. Schuhmann and U. Apfel, Influence of the Fe:Ni Ratio and Reaction Temperature on the Efficiency of (Fe<sub>x</sub>Ni<sub>1-x</sub>)<sub>9</sub>S<sub>8</sub> Electrocatalysts Applied in the Hydrogen Evolution Reaction, *ACS Catal.*, 2017, **8**(2), 987–996.

29 E. J. Dufek, T. E. Lister and M. E. McIlwain, Bench-Scale Electrochemical System for Generation of CO and Syn-Gas, *J. Appl. Electrochem.*, 2011, **41**(6), 623–631.

30 Z. Yin, H. Peng, X. Wei, H. Zhou, J. Gong, M. Huai, L. Xiao, G. Wang, J. Lu and L. Zhuang, An Alkaline Polymer Electrolyte CO<sub>2</sub> Electrolyzer Operated with Pure Water, *Energy Environ. Sci.*, 2019, **12**(8), 2455–2462.

31 K. Li, S. Zou, J. Zhang, Y. Huang, L. He and X. Feng, Superhydrophobicity-Enabled Efficient Electrocatalytic CO<sub>2</sub> Reduction at High Temperature, *ACS Catal.*, 2023, **13**(14), 9346–9351.

32 M. E. Boot-Handford, J. C. Abanades, E. J. Anthony, M. J. Blunt, S. Brandani, N. Mac Dowell, J. R. Fernández, M. Ferrari, R. Gross, J. P. Hallett, R. S. Haszeldine, P. Heptonstall, A. Lyngfelt, Z. Makuch, E. Mangano, R. T. J. Porter, M. Pourkashanian, G. T. Rochelle, N. Shah and P. S. Fennell, Carbon Capture and Storage Update, *Energy Environ. Sci.*, 2013, **7**(1), 130–189.

33 D. Corral, J. T. Feaster, S. Sobhani, J. R. DeOtte, D. U. Lee, A. A. Wong, J. Hamilton, V. A. Beck, A. Sarkar, C. Hahn,



T. F. Jaramillo, S. E. Baker and E. B. Duoss, Advanced Manufacturing for Electrosynthesis of Fuels and Chemicals from CO<sub>2</sub>, *Energy Environ. Sci.*, 2021, **14**(5), 3064–3074.

34 H. Simonson, W. E. Klein, D. Henckel, S. Verma, K. C. Neyerlin and W. A. Smith, Direct Measurement of Electrochemical Selectivity Gradients over a 25 cm<sup>2</sup> Copper Gas Diffusion Electrode, *ACS Energy Lett.*, 2023, **8**(9), 3811–3819.

35 J. Li, Z. Wang, C. McCallum, Y. Xu, F. Li, Y. Wang, C. M. Gabardo, C. T. Dinh, T.-T. Zhuang, L. Wang, J. Y. Howe, Y. Ren, E. H. Sargent and D. Sinton, Constraining CO Coverage on Copper Promotes High-Efficiency Ethylene Electroproduction, *Nat. Catal.*, 2019, **2**(11), 1124–1131.

36 H. Wu, B. Tian, W. Xu, K. K. Abdalla, Y. Kuang, J. Li and X. Sun, Pressure-Dependent CO<sub>2</sub> Electroreduction to Methane over Asymmetric Cu–N<sub>2</sub> Single-Atom Sites, *J. Am. Chem. Soc.*, 2024, **146**(32), 22266–22275.

37 C. A. G. Rodriguez, N. C. Kani, A. B. Moss, B. O. Joensen, S. Garg, W. Deng, T. Wilson, J. R. Varcoe, I. Chorkendorff and B. Seger, Insights into Zero-Gap CO<sub>2</sub> Electrolysis at Elevated Temperatures, *EES Catal.*, 2024, **2**(3), 850–861.

38 X. She, L. Zhai, Y. Wang, P. Xiong, M. M. Li, T. Wu, M. C. Wong, X. Guo, Z. Xu, H. Li, H. Xu, Y. Zhu, S. C. E. Tsang and S. P. Lau, Pure-Water-Fed Electrocatalytic CO<sub>2</sub> Reduction to Ethylene Beyond 1000 h Stability at 10 A, *Nat. Energy*, 2024, **9**(1), 81–91.

39 R. E. Vos, J. P. Smaak and M. T. M. Koper, The Temperature Dependence of Electrochemical CO<sub>2</sub> Reduction on Ag and CuAg Alloys, *J. Catal.*, 2024, **436**(1), 115613.

40 A. Löwe, C. Rieg, T. Hierlemann, N. Salas, D. Kopljarić, N. Wagner and E. Klemm, Influence of Temperature on the Performance of Gas Diffusion Electrodes in the CO<sub>2</sub> Reduction Reaction, *ChemElectroChem*, 2019, **6**(17), 4497–4506.

41 M. R. Singh, J. D. Goodpaster, A. Z. Weber, M. Head-Gordon and A. T. Bell, Mechanistic Insights into Electrochemical Reduction of CO<sub>2</sub> over Ag Using Density Functional Theory and Transport Models, *Proc. Natl. Acad. Sci. U. S. A.*, 2017, **114**(42), E8812–E8821.

42 X. Zhu, J. Huang and M. Eikerling, Electrochemical CO<sub>2</sub> Reduction at Silver from a Local Perspective, *ACS Catal.*, 2021, **11**(23), 14521–14532.

43 D. M. Koshy, S. S. Nathan, A. S. Asundi, A. M. Abdellah, S. M. Dull, D. A. Cullen, D. Higgins, Z. Bao, S. F. Bent and T. F. Jaramillo, Bridging Thermal Catalysis and Electrocatalysis: Catalyzing CO<sub>2</sub> Conversion with Carbon-Based Materials, *Angew. Chem., Int. Ed.*, 2021, **60**(32), 17472–17480.

44 P. Mardle, S. Cassegrain, F. Habibzadeh, Z. Shi and S. Holdcroft, Carbonate Ion Crossover in Zero-Gap, KOH Anolyte CO<sub>2</sub> Electrolysis, *J. Phys. Chem. C*, 2021, **125**(46), 25446–25454.

45 J. Y. Kim, P. Zhu, F. Chen, Z. Wu, D. A. Cullen and H. Wang, Recovering Carbon Losses in CO<sub>2</sub> Electrolysis Using a Solid Electrolyte Reactor, *Nat. Catal.*, 2021, **5**(4), 288–299.

46 A. B. Moss, S. Garg, M. Mirolo, C. A. G. Rodriguez, R. Ilvonen, I. Chorkendorff, J. Drnec and B. Seger, In Operando Investigations of Oscillatory Water and Carbonate Effects in MEA-Based CO<sub>2</sub> Electrolysis Devices, *Joule*, 2023, **7**(2), 350–365.

47 L. Weng, A. T. Bell and A. Z. Weber, Towards Membrane-Electrode Assembly Systems for CO<sub>2</sub> Reduction: A Modeling Study, *Energy Environ. Sci.*, 2019, **12**(6), 1950–1968.

48 M. C. O. Monteiro, F. Dattila, N. López and M. T. M. Koper, The Role of Cation Acidity on the Competition between Hydrogen Evolution and CO<sub>2</sub> Reduction on Gold Electrodes, *J. Am. Chem. Soc.*, 2021, **144**(4), 1589–1602.

49 J. E. Huang, F. Li, A. Ozden, A. S. Rasouli, F. P. G. De Arquer, S. Liu, S. Zhang, M. Luo, X. Wang, Y. Lum, Y. Xu, K. Bertens, R. K. Miao, C. Dinh, D. Sinton and E. H. Sargent, CO<sub>2</sub> Electrolysis to Multicarbon Products in Strong Acid, *Science*, 2021, **372**(6546), 1074–1078.

50 J. Gu, S. Liu, W. Ni, W. Ren, S. Haussener and X. Hu, Modulating Electric Field Distribution by Alkali Cations for CO<sub>2</sub> Electroreduction in Strongly Acidic Medium, *Nat. Catal.*, 2022, **5**(4), 268–276.

51 J. Hou, B. Xu and Q. Lu, Influence of Electric Double Layer Rigidity on CO Adsorption and Electroreduction Rate, *Nat. Commun.*, 2024, **15**, 1926.

52 Y. Xu, J. P. Edwards, S. Liu, R. K. Miao, J. E. Huang, C. M. Gabardo, C. P. O'Brien, J. Li, E. H. Sargent and D. Sinton, Self-Cleaning CO<sub>2</sub> Reduction Systems: Unsteady Electrochemical Forcing Enables Stability, *ACS Energy Lett.*, 2021, **6**(2), 809–815.

53 B. Siritanaratkul, M. Förster, F. Greenwell, P. K. Sharma, E. H. Yu and A. J. Cowan, Zero-GAP Bipolar Membrane Electrolyzer for Carbon Dioxide Reduction Using Acid-Tolerant Molecular Electrocatalysts, *J. Am. Chem. Soc.*, 2022, **144**(17), 7551–7556.

54 K. Yang, M. Li, S. Subramanian, M. A. Blommaert, W. A. Smith and T. Burdyny, Cation-Driven Increases of CO<sub>2</sub> Utilization in a Bipolar Membrane Electrode Assembly for CO<sub>2</sub> Electrolysis, *ACS Energy Lett.*, 2021, **6**(12), 4291–4298.

55 J. Wang, Y. Zhao, B. P. Setzler, S. Rojas-Carbonell, C. B. Yehuda, A. Amel, M. Page, L. Wang, K. Hu, L. Shi, S. Gottesfeld, B. Xu and Y. Yan, Poly(aryl piperidinium) membranes and ionomers for hydroxide exchange membrane fuel cells, *Nat. Energy*, 2019, **4**(5), 392–398.

56 S. Weng, W. L. Toh and Y. Surendranath, Weakly coordinating organic cations are intrinsically capable of supporting CO<sub>2</sub> reduction catalysis, *J. Am. Chem. Soc.*, 2023, **145**(30), 16787–16795.

57 J. McGregor, J. T. Bender, A. S. Petersen, L. Cañada, J. Rossmeisl, J. F. Brennecke and J. Resasco, Organic electrolyte cations promote non-aqueous CO<sub>2</sub> reduction by mediating interfacial electric fields, *Nat. Catal.*, 2025, **8**(1), 79–91.

58 S. Chen, J. Liu, Q. Zhang, F. Teng and B. C. McLellan, A Critical Review on Deployment Planning and Risk Analysis of Carbon Capture, Utilization, and Storage (CCUS) Toward Carbon Neutrality, *Renewable Sustainable Energy Rev.*, 2022, **167**, 112537.

59 A. Raksajati, M. T. Ho and D. E. Wiley, Reducing the Cost of CO<sub>2</sub> Capture from Flue Gases Using Aqueous Chemical Absorption, *Ind. Eng. Chem. Res.*, 2013, **52**(47), 16887–16901.



60 G. V. Last and M. T. Schmick, A Review of Major Non-Power-Related Carbon Dioxide Stream Compositions, *Environ. Earth Sci.*, 2015, **74**(2), 1189–1198.

61 Y. Liu, J. Huang, H. Zhu, P. Liao and X. Chen, Simultaneous Capture of CO<sub>2</sub> Boosting Its Electroreduction in the Micropores of a Metal–Organic Framework, *Angew. Chem., Int. Ed.*, 2023, **62**, e202311265.

62 Z. Wang, Y. Zhou, D. Liu, R. Qi, C. Xia, M. Li, B. You and B. Y. Xia, Carbon-Confining Indium Oxides for Efficient Carbon Dioxide Reduction in a Solid-State Electrolyte Flow Cell, *Angew. Chem., Int. Ed.*, 2022, **61**, e202200552.

63 Z. Zhao, J. Huang, D. Huang, H. Zhu, P. Liao and X. Chen, Efficient Capture and Electroreduction of Dilute CO<sub>2</sub> into Highly Pure and Concentrated Formic Acid Aqueous Solution, *J. Am. Chem. Soc.*, 2024, **146**(20), 14349–14356.

64 D. Kim, W. Choi, H. W. Lee, S. Y. Lee, Y. Choi, D. K. Lee, W. Kim, J. Na, U. Lee, Y. J. Hwang and D. H. Won, Electrocatalytic Reduction of Low Concentrations of CO<sub>2</sub> Gas in a Membrane Electrode Assembly Electrolyzer, *ACS Energy Lett.*, 2021, **6**(10), 3488–3495.

65 R. F. Service, Cost of carbon capture drops, but does anyone want it?, *Science*, 2016, **354**(6318), 1362–1363.

